PROCEEDINGS OF SPIE

SPIEDigitalLibrary.org/conference-proceedings-of-spie

The large area detector onboard the eXTP mission

Marco Feroci, Giovanni Ambrosi, Filippo Ambrosino, Matias Antonelli, Andrea Argan, et al.

Marco Feroci, Giovanni Ambrosi, Filippo Ambrosino, Matias Antonelli, Andrea Argan, Viktor Babinec, Marco Barbera, Joerg Bayer, Pierluigi Bellutti, Bruna Bertucci, Giuseppe Bertuccio, Xingzi Bi, Mirko Boezio, Valter Bonvicini, Giacomo Borghi, Enrico Bozzo, David Baudin, Florent Bouyjou, Daniele Brienza, Franck Cadoux, Riccardo Campana, Jiewei Cao, Elisabetta Cavazzuti, Francesco Ceraudo, Tianxiang Chen, Wen Chen, Daniela Cirrincione, Nicolas De Angelis, Alessandra De Rosa, Ettore Del Monte, Sergio Di Cosimo, Giuseppe Dilillo, Roman Dohnal, Immacolata Donnarumma, Yuri Evangelista, Qingmei Fan, Yannick Favre, Emanuele Fiandrini, Francesco Ficorella, Fabio Fuschino, Na Gao, Olivier Gevin, Marco Grassi, Manuel Guedel, Xingbo Han, Huilin He, Paul Hedderman, Jan-Willem den Herder, Richard Hynek, Bin Hong, Ge Jin, Merlin Kole, Vladimir Karas, Martin Komarek, Claudio Labanti, Loghui Li, Tianming Li, Hong Liang, Olivier Limousin, Rui Liu, Ugo Lo Cicero, Jens Lohering, Giovanni Lombardi, Fang-Jun Lu, Tao Luo, Piero Malcovati, Hanqi Mao, Andrea Marinucci, Filippo Mele, Vasco Mendes, Martin Merkl, Aline Meuris, Malgorzata Michalska, Alfredo Morbidini, Gianluca Morgante, Fabio Muleri, Riccardo Munini, Lorenzo Mussolin, Barbara Negri, Petr Novák, Witold Nowosielski, Alessio Nuti, Piotr Orleanski, Roland Ottensamer, Luigi Pacciani, Stephane Paltani, Teng Pan, Giancarlo Pepponi, Emanuele Perinati, Raffaele Piazzolla, Antonino Picciotto, Samuel Pliego, Alexandre Rachevski, Irina Rashevskaia, Andrea Santangelo, Stéphane Schanne, Roberto Serafinelli, Konrad Skup, Libor Sveda, Jiri Svoboda, Chris Tenzer, Michela Todaro, Gabriel Torok, Alessio Trois, Andrea Vacchi, Enrico Virgilli, Hao Xiong, Jian Wang, Xianqi Wang, Berend Winter, Xin Wu, Yupeng Xu, Ganluigi Zampa, Nicola Zampa, Andrzej A. Zdziarski, Long Zhang, Shu Zhang, Shuang-Nan Zhang, Wenda Zhang, Xiaoli Zhang, Zhen Zhang, Yupeng Zhou, Nicola Zorzi, "The large area detector onboard the eXTP mission," Proc. SPIE 12181, Space Telescopes and Instrumentation 2022: Ultraviolet to Gamma Ray, 121811X (31 August 2022); doi: 10.1117/12.2628814

SPIE.

Event: SPIE Astronomical Telescopes + Instrumentation, 2022, Montréal, Québec, Canada

The Large Area Detector onboard the eXTP mission

Marco Feroci*[a,b], Giovanni Ambrosi[d], Filippo Ambrosino[a], Matias Antonelli[z], Andrea Argan[a,ii], Viktor Babinec[cc], Marco Barbera[e,f], Joerg Bayer[g], Pierluigi Bellutti[h], Bruna Bertucci[i], Giuseppe Bertuccio[c], Xingzi Bi[hh], Mirko Boezio[z], Walter Bonvicini[z], Giacomo Borghi[h], Enrico Bozzo[l], David Baudin[o], Florent Bouyjou[o], Daniele Brienza[dd], Franck Cadoux[m], Riccardo Campana[n], Jiewei Cao[p], Elisabetta Cavazzuti[dd], Francesco Ceraudo[a], Tianxiang Chen[p], Wen Chen[hh], Daniela Cirrincione[q,z], Nicolas De Angelis[m], Alessandra De Rosa[a], Ettore Del Monte[a,b], Sergio Di Cosimo[a], Giuseppe Dilillo[a], Roman Dohnal[cc], Immacolata Donnarumma[dd], Yuri Evangelista[a,b], Qingmei Fan[zz], Yannick Favre[m], Emanuele Fiandrini[i], Francesco Ficorella[h], Fabio Fuschino[n], Na Gao[p], Olivier Gevin[o], Marco Grassi[r], Manuel Guedel[ee], Xingbo Han[hh], Huilin He[p], Paul Hedderman[g], Jan-Willem den Herder[gg], Richard Hynek[cc], Bin Hong[zz], Ge Jin[s], Merlin Kole[m], Vladimir Karas[t], Martin Komarek[cc], Claudio Labanti[n], Loghui Li[s], Tianming Li[p], Hong Liang[hh], Olivier Limousin[o], Rui Liu[hh], Ugo Lo Cicero[f], Jens Loehring[aa], Giovanni Lombardi[a], Fang-Jun Lu[p], Tao Luo[p], Piero Malcovati[r], Hanqi Mao[s], Andrea Marinucci[dd], Filippo Mele[c], Vasco Mendes[ff], Martin Merkl[cc], Aline Meuris[o], Malgorzata Michalska[w], Alfredo Morbidini[a], Gianluca Morgante[n], Fabio Muleri[a,b], Riccardo Munini[z], Lorenzo Mussolin[i], Barbara Negri[dd], Petr Novák[bb], Witold Nowosielski[w], Alessio Nuti[a], Piotr Orleanski[w], Roland Ottensamer[ee], Luigi Pacciani[a], Stephane Paltani[l], Teng Pan[zz], Giancarlo Pepponi[h], Emanuele Perinati[g], Raffaele Piazzolla[dd], Antonino Picciotto[h], Samuel Pliego[g], Alexandre Rachevski[z], Irina Rashevskaia[x], Andrea Santangelo[g], Stephane Schanne[o], Roberto Serafinelli[a], Konrad Skup[w], Libor Sveda[t], Jiri Svoboda[t], Chris Tenzer[g], Michela Todaro[e,f], Gabriel Torok[ij], Alessio Trois[ff], Andrea Vacchi[q,z], Enrico Virgilli[n], Hao Xiong[g], Jian Wang[s], Xianqi Wang[g], Berend Winter[u], Xin Wu[m], Yupeng Xu[p], Ganluigi Zampa[z], Nicola Zampa[z], Andrzej A. Zdziarski[y], Long Zhang[zz], Shu Zhang[p], Shuang-Nan Zhang[p], Wenda Zhang[t], Xiaoli Zhang[zz], Zhen Zhang[s], Yupeng Zhou[zz], Nicola Zorzi[h]

[a]INAF, Istituto di Astrofisica e Planetologia Spaziali, Via Fosso del Cavaliere 100, 00133 Rome, Italy; [b]INFN, Sezione Roma Tor Vergata, Via della Ricerca Scientifica, 00133, Rome, Italy;

[c]Politecnico di Milano, Polo di Como, Via Anzani 41, Como, Italy; [d]INFN, Sezione di Perugia, Via Alessandro Pascoli, 23c, 06123, Perugia, Italy; [e]Università di Palermo, Dipartimento di Fisica e Chmica, Via Archirafi 36, 90123, Palermo, Italy; [f]INAF, Osservatorio Astronomico di Palermo, Piazza del Parlamento, 1, 90134, Palermo, Italy; [g]Institut fur Astronomie und Astrophysik, Eberhard Karls Universitat, 72076 Tuebingen, Germany; [h]Fondazione Bruno Kessler, Via Sommarive, Povo, 38123, Trento, Italy; [i]University of Perugia, Dip. Fisica e Geologia, Via Pascoli snc - 06123 - Perugia Italy; [l]Department of Astronomy, University of Geneva, Chemin d'Ecogia 16, 1290, Versoix, Switzerland; [m]Department of Nuclear and Particle Physics, University of Geneva, CH-1205, Switzerland; [n]INAF, Osservatorio di astrofisica e scienza dello spazio di Bologna, Via P. Gobetti 101, Bologna, Italy; [o]CEA Paris-Saclay, DRF/IRFU, 91191 Gif sur Yvette, France

[p]Key Laboratory for Particle Astrophysics, Institute of High Energy Physics, CAS, Beijing 100049, China; [q]University of Udine, Via delle Scienze, 206, 33100, Udine, Italy; [r]University of Pavia, Department of Electrical, Computer, and Biomedical Engineering, Via Ferrata 5, 27100 Pavia, Italy

[s]North Night Vision Technology Co. Ltd, Nanjing 211106, China; [t]Astronomical Institute, Czech Academy of Sciences, Bocni II 1401, CZ-14100 Prague, Czech Republic; [u]Mullard Space Science Laboratory, UCL, Holmbury St Mary, Dorking, Surrey, RH56NT, UK; [v]Space Research Centre, Department of Physics and Astronomy, University of Leicester, Leicester, LE17RH, UK

[w]Space Research Center, Polish Academy of Sciences, Bartycka 18a, 00-716 Warszawa, Poland

Space Telescopes and Instrumentation 2022: Ultraviolet to Gamma Ray, edited by Jan-Willem A. den Herder, Shouleh Nikzad, Kazuhiro Nakazawa, Proc. of SPIE Vol. 12181, 121811X · © 2022 SPIE · 0277-786X · doi: 10.1117/12.2628814

[x]TIFPA, Istituto Nazionale di Fisica Nucleare, Via Sommarive 14, 38123 Povo, Trento, Italy [y]Nicolaus Copernicus Astronomical Center, Polish Academy of Sciences, Bartycka 18, PL-00-716 Warszawa, Poland; [z]INFN, Sezione di Trieste, Padriciano 99, 34149, Italy; [zz]Beijing Institute of Spacecraft System Engineering, CAST, Beijing 10094, China; [aa]European Space Agency, Keplerlaan 1, PO Box 299 NL-2200 AG Noordwijk, The Netherlands; [bb]Frentech Aerospace s.r.o. Jarní 48 CZ S 614 00 Brno; [cc]L.K. Engineering, s.r.o. Vídenská 55 63900 Brno Czech Republic; [dd]Italian Space Agency, Via del Politecnico snc, 00133 Rome, Italy; [ee]Universität Wien, Universitätsring 1, 1010 Wien, Austria; [ff]INAF – Osservatorio Astronomico di Cagliari, Via della Scienza 5 - 09047 Selargius (CA), Italy; [gg]SRON Netherlands Institute for Space Research, NL-2333 CA Leiden, the Netherlands; [hh]Innovation Academy for Microsatellites of CAS, Xueyang Road No.1, Pudong district, Shanghai, China; [ii]INAF, Viale del Parco Mellini 84, I-00136 Rome, Italy; [jj]Institute of Physics, Silesian University in Opava, Bezrucovo nam. 13, CZ-746 01 Opava, Czech Republic

*marco.feroci@inaf.it

ABSTRACT

The Large Area Detector (LAD) is the high-throughput, spectral-timing instrument onboard the eXTP mission, a flagship mission of the Chinese Academy of Sciences and the China National Space Administration, with a large European participation coordinated by Italy and Spain. The eXTP mission is currently performing its phase B study, with a target launch at the end-2027. The eXTP scientific payload includes four instruments (SFA, PFA, LAD and WFM) offering unprecedented simultaneous wide-band X-ray timing and polarimetry sensitivity. The LAD instrument is based on the design originally proposed for the LOFT mission. It envisages a deployed 3.2 m^2 effective area in the 2-30 keV energy range, achieved through the technology of the large-area Silicon Drift Detectors - offering a spectral resolution of up to 200 eV FWHM at 6 keV - and of capillary plate collimators - limiting the field of view to about 1 degree. In this paper we will provide an overview of the LAD instrument design, its current status of development and anticipated performance.

1. INTRODUCTION

The enhanced X-ray Timing and Polarimetry mission (eXTP) is a flagship mission of China, with a large contribution by a European consortium, including institutions in Italy, Spain, Austria, Czech Republic, Denmark, France, Germany, the Netherlands, Poland, Switzerland and Turkey. The eXTP mission is being designed to address the science themes of understanding the behavior of matter under extreme conditions of gravity, density and magnetism. eXTP aims at determining the equation of state of ultra-dense matter in the interior of neutron stars, study the dynamics of matter in the vicinity of neutron stars and near the event horizon of black holes - where the General Relativity theory predicts large distorsions of the space-time with respect to a Newton's laws – and study the effects on the propagation of photons of the ultra-critical magnetic fields hosted in magnetar sources. These science goals will be achieved through a payload enabling - for the first time ever – high-throughput, simultaneous spectral, timing and polarimetry observations of the same target sources. An extensive description of the eXTP science case was provided in a set of four papers discussing Dense matter[2], Accretion in strong field gravity[3], Strong magnetism[4] and Observatory science[5]. An update of the eXTP science case is being prepared by the eXTP Science Working Groups, in light of the new observational results achieved in this field by the science community, especially with respect to the multi-messenger astronomy and the recent X-ray polarimetry results published by the IXPE satellite[1].

The scientific instruments onboard eXTP are the Spectroscopy Focusing Array (SFA, a set of 9 telescopes equipped with Silicon Drift Detectors, reaching a maximum effective area of ~0.5 m^2 at 1 keV and <180 eV FWHM spectral resolution at 6 keV), the Polarimetry Focusing Array (PFA, a set of 4 telescopes equipped with the polarization-sensitive Gas Pixel Detectors, reaching an effective area 5 times larger than the polarimeter onboard the IXPE mission[6]), the Wide Field Monitor (WFM, a coded mask instrument simultaneously imaging ~1/3 of the sky, with arcmin resolution[7]) and the

Large Area Detector (LAD), the subject of this paper. The eXTP instruments are designed to be fully complementary: the SFA provides the soft response (down to 0.5 keV) and the low background obtained by focusing X-rays onto small detectors, the LAD offers the largest effective area ever achieved at the Fe line energy and the hard response up to 30 keV, the PFA enables the polarization sensitivity in the 2-10 keV range, while the large field of view and angular resolution of the WFM will be crucial for triggering the target sources in their most interesting states and discover new transients. The eXTP spacecraft is being designed by the Microsat company in China. A thorough description of the eXTP mission and scientific payload is provided in Zhang et al.[8,9]. In Figure 1 we show its current configuration[21], with the allocation of the four scientific instruments.

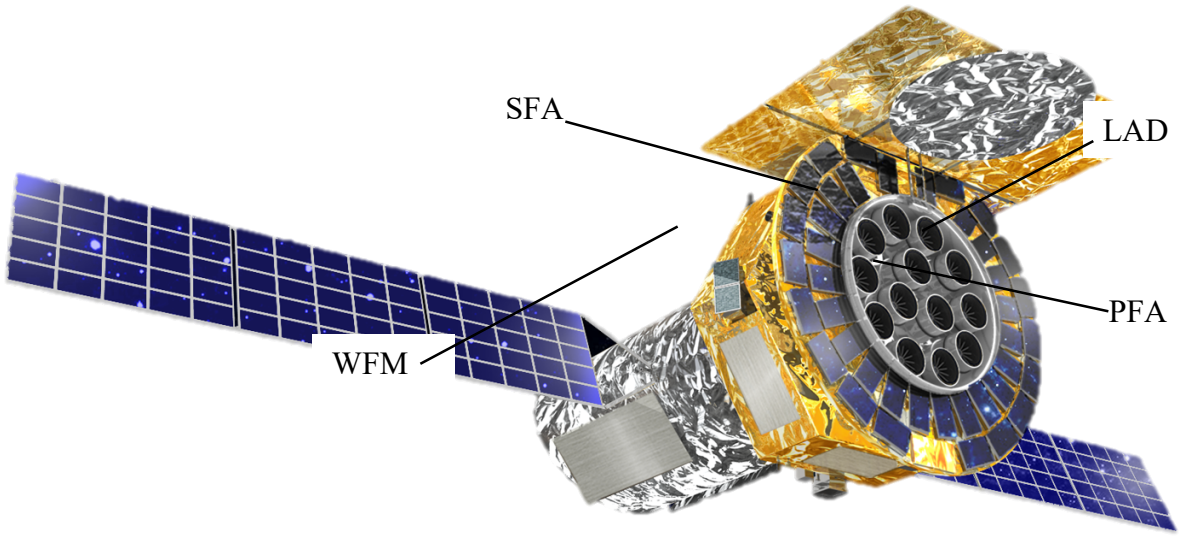

Figure 1 The current configuration of the eXTP satellite, showing the accommodation of the four instruments of the scientific payload.

2. LAD INSTRUMENT OVERVIEW

The LAD is designed to be the most sensitive spectral-timing instrument for bright Galactic and extragalactic sources to date. As we will discuss in the next sections, an innovative and highly efficient technology and design allow to deploy in space an effective area as large as 3.2 m^2 at 8 keV, adopting a modular configuration. This is 6x larger than the largest X-ray instruments flown so far, PCA onboard RXTE and LAXPC onboard ASTROSAT, as shown in Figure 2. In contrast to its predecessors, the LAD combines the large effective area with the spectral resolution typical of solid-state detectors, reaching a required energy resolution of 260 eV FWHM at 6 keV, thus opening for the first time the new window of high-throughput, spectral-timing for bright sources. In fact, the largest instrument with spectral resolution in the same class is XMM-Newton, which has an effective area >30x lower than the LAD and is not optimized for bright sources (whereas the LAD is not optimized for dim sources, though).

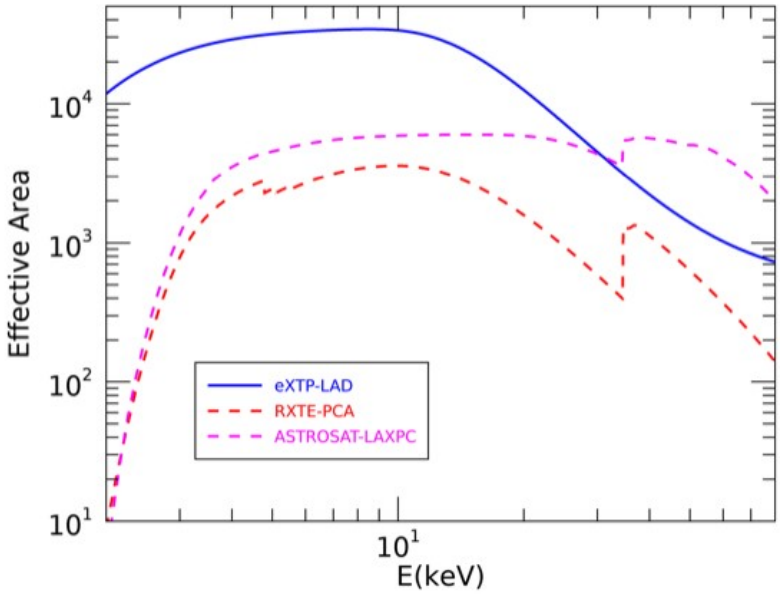

Figure 2 The eXTP LAD effective area, as compared to the past PCA experiment onboard RXTE and the LAXPC experiment onboard the ASTROSAT mission

The LAD is a large area, collimated instrument (1° field of view, FWHM). This design reduces to negligible levels the dead-time and pile-up effects. In fact, as an example, the rate of each of the ~144,000 channels of the LAD when observing the Crab Nebula is just ~1 count/s. As a drawback of this design, the background is higher than in focusing instruments (e.g., the SFA onboard the same payload), making the LAD an excellent instrument primarily for bright sources (above the intensity of a few mCrab). The impact of the LAD on the field will be boosted further by the simultaneous observation of the same sources by the other instruments of the eXTP payload suite, enabling combined spectral-timing-polarimetry diagnostics of sources, as well as compensating for limits of the instrument (e.g., the imaging capabilities of WFM and PFA will allow to detect contaminating sources in the collimated field of view of the LAD). The main features of the LAD are listed in Table 1.

Table 1 The main features of the LAD instrument

Parameter	Value
Energy Range	2-30 keV nominal 2-80 keV extended
Effective Area	>1.3 m^2 @ 2 keV >3 m^2 @ 8 keV >1.5 m^2 @ 30 keV
Energy Resolution	<260 eV FWHM @ 6 keV (all events)
Field of View	<65 arcmin FWHM
Field of Regard	>50%
Time Resolution	10 μs
Absolute Time Accuracy	2 μs
Dead Time	<1% @1Crab
Maximum Flux (sustained)	>1 Crab
Maximum Flux (time-limited)	>15 Crab (300 minutes)
Total Mass	571 kg CBE+DMM
Total Power	769 W CBE+DMM
Telemetry	1 Mbps (typical, for a 250 mCrab source)

The LAD is organized as a modular instrument, composed of 40 coaligned Modules, each one hosting a set of 16 large area Silicon Drift Detectors (SDDs) and 16 corresponding capillary plate collimators. The 40 Modules are hierarchically interfaced by a set of 4 Panel Back End Electronics (PBEE), each one supporting 10 Modules, that are in turn interfaced to an Instrument Control Unit, in cold redundancy. Figure 3 shows the architecture of the LAD instrument, in a geometry mimicking the accommodation on the spacecraft.

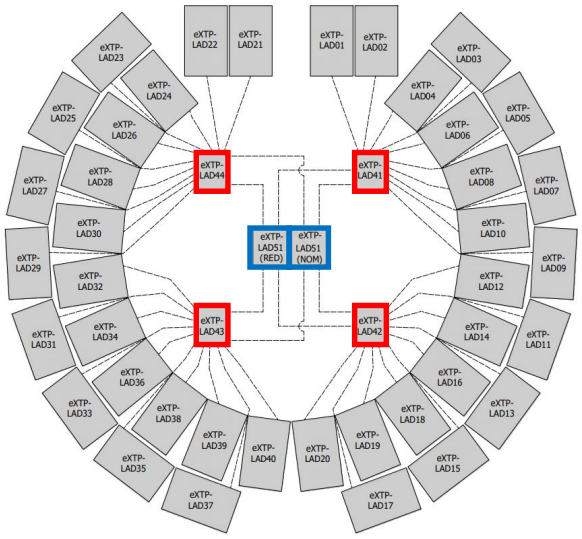

Figure 3 The architecture of the LAD experiment, in a geometry mimicking the accommodation on the spacecraft. The 40 gray boxes are the Modules, the 4 red boxes are the PBEEs and the 2 blue boxes are the ICUs.

3. INSTRUMENT DESIGN AND PROTOTYPING

The Module is at the heart of the LAD instrument. It is a self-consistent subsystem hosting the sensitive components of the instrument (the SDDs) and their Front-End Electronics (FEE), Module Back-End Electronics (MBEE) and Power Supplies (PSU), as well as components defining the optical design of the instrument, the capillary plate collimators and the optical filters. The design of the Module is shown in Figure 4. The instrument is conceptually organized in two halves: the detector tray and the collimator tray. The detector tray is a frame structure (Detector Frame) that guarantees the thermomechanical support and interface to the 16 Detector Assemblies (DAs), the 2 MBEEs and the 2 Power Supply Units (PSUs). The Detector Assemblies are in turn composed of the SDD, the FEE (hosting the read-out ASICs) and their H-shaped mechanical support frame. The Detector Tray assembly is shown with an exploded view in the upper part of the bottom panel of Figure 4. The backside of the Detector Tray is covered with a Lead shield, to prevent background photons reaching the detectors from the back of the Module, and a radiator, contributing to radiate the heat generated by the power dissipated inside the Module. The Collimator Tray is the thermomechanical structure holding the 16 capillary plate collimators and the 16 optical filters in place. The Collimator Tray has the task to keep the collimators co-aligned to within ~1 arcmin regardless of the environmental conditions during the launch and the nominal operational phase. To achieve this, a special clamping mechanism has been designed, allowing for the differential thermal expansion of the capillary plates (made of Lead glass) and the tray (made of Aluminum). The exploded view of the Collimator Tray is shown at the bottom part of the bottom panel of Figure 4. As shown in Figure 1, the 40 Modules are hosted in a dedicated truss structure of the spacecraft, forming a corona around the mirror modules of the SFA and PFA instruments. The interface between the truss and the Modules is kinematical (two of the three kinematical interfaces are visible in Figure 4, top panel) in order to improve the coalignment among the Modules and the alignment between the 40 Modules and the satellite boresight. The total requirement for the alignment is 2.1 arcmin. The top panel of Figure 4 also shows the 6 optical cubes of the Module that allow to measure the alignment during each phase of the AIVT and calibration process.

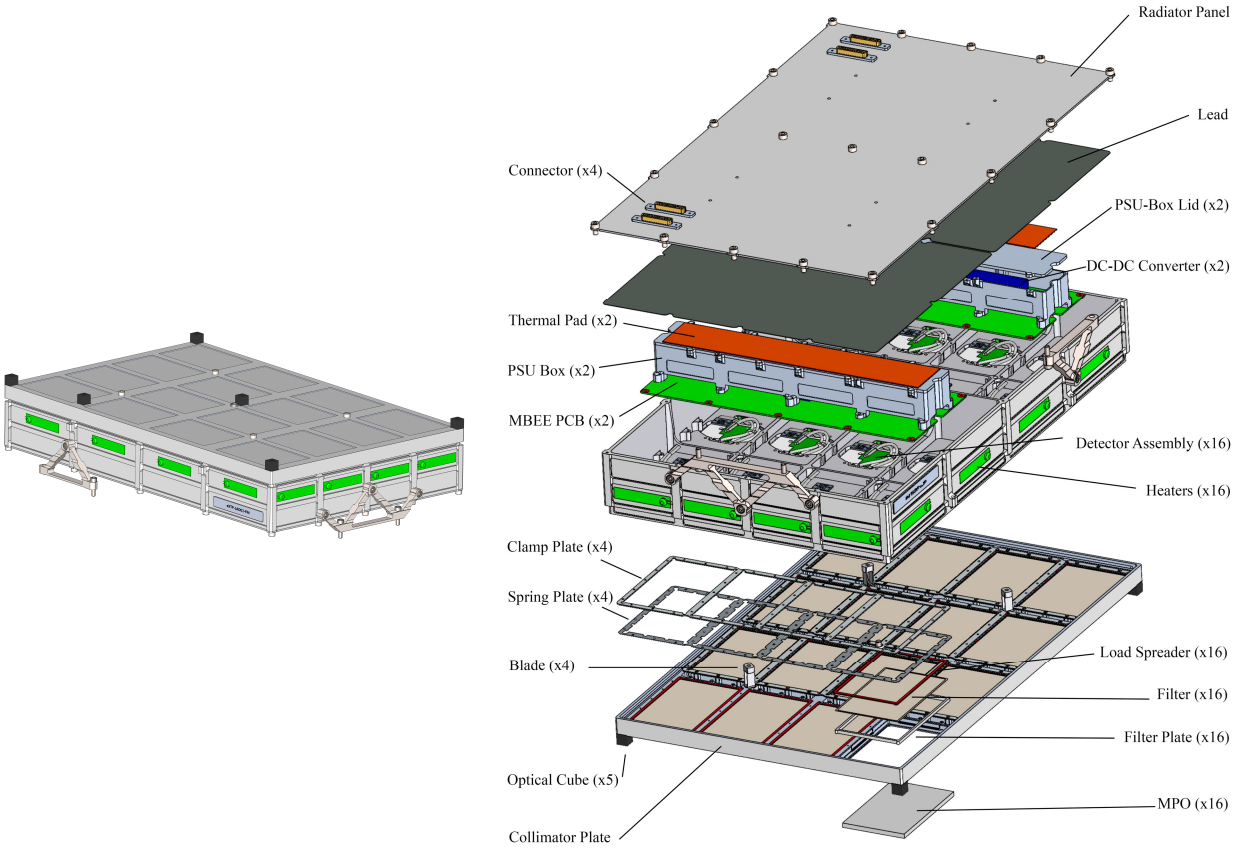

Figure 4 The current design of the LAD Module. The figure on the left shows the Module in the assembled configuration. The figure on the right shows an exploded view, with specification of the main components and subsystems.

3.1 The Module components

Detector Assembly

The Detector Assembly (DA, Figure 5) is a "sandwich" including the SDD and the FEE, together with their mechanical support. The SDD is a monolithic, 87 cm^2 (active: 76 cm^2), 450 µm thick Silicon detector[10,11]. The drift field is guaranteed by 1300 V high voltage applied at the middle plane of the detector, with the 112 anodes reading out the charge being polarized to ground. The electrons created by the absorption of an X-ray photon in the Silicon bulk are thus drifted towards one of the two long edges of the SDD tile and read-out by one or two anodes, depending on the absorption point along the drift channel and with respect to the 970 µm anode pitch, due to the charge diffusion during the drift.

The LAD SDD detectors are being jointly developed by INFN, FBK, ASI and INAF. Full scale prototypes have already been produced and are undergoing performance test campaigns.

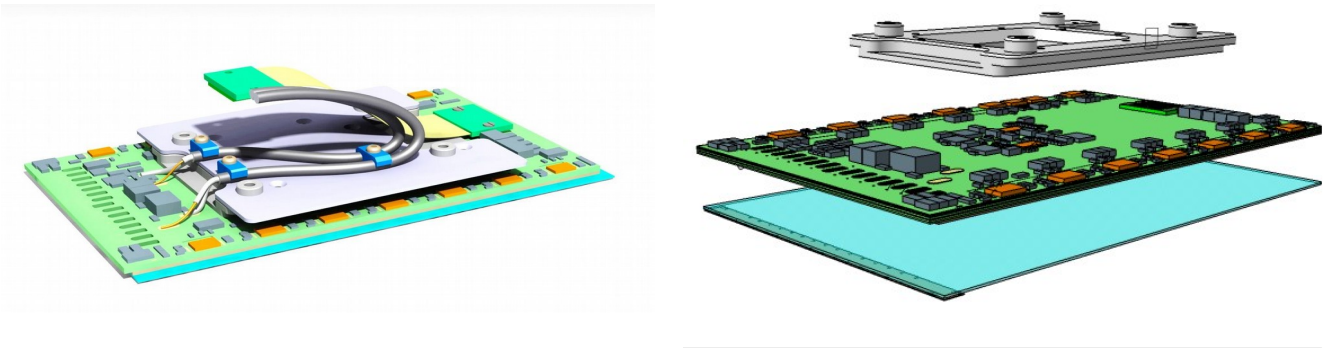

Figure 5 The current design of the LAD Detector Assembly carried out at DPNC (University of Geneve), including the detector, the front-end electronics and the mechanical interface. The left panel shows the Detector Assembly integrated, while the right panel shows an exploded view.

The analogue readout of the SDD signal is performed by a set of 28 IDeF-X ASICs[13], 14 on each side. Each ASIC has indeed 32 channels at a 150 µm pitch, but the pitch mismatch with the detector allows to connect only 8 channels per ASIC. The output of the 28 IDeF-X ASICs is fed into two OWB-1 ASICs[14], in charge of the A/D conversion at 13-bit resolution. The two OWB-1 serve one side of the detector each. Both the analogue and digital ASICs were developed in the AMS 0.35µm technology.

The ASICs and the other components are hosted on an FR4 printed circuit board (PCB), directly glued to the SDD, thus representing also a mechanical support structure for it. The size of the PCB is designed to be slightly smaller than the SDD size on the long edges, thus allowing for a direct wire bonding from the SDD anodes to the ASIC input pads, located on top of the PCB. Additional wire bondings pass through dedicated holes of the PCB to reach the SDD cathodes biased to control the drift field for the electrons. The side of the PCB opposite to the SDD is glued to an H-shaped mechanical pad with the multiple purpose of providing mechanical stiffness, a screw interface to the Detector Tray, offering a low-impedance path to the heat generated by the front-end electronics and protecting ASICs and wire bondings during the assembly procedures. The FEE has three interconnections to the MBEE and PSU: a flat cable for the signals and two coaxial cables for the high voltage and low voltage power supply.

A dedicated ASIC development program is ongoing at CEA (Saclay) to adapt and improve the characteristics and performance of the IDeF-X ASIC to the LAD requirements. An early prototype, IDeF-X HDBD was already developed and tested[13]. A newer and further improved prototype was developed in 2021 and it is currently under test at the CEA laboratories.

Module Back End Electronics and Power Supply Units

The Detector Assemblies in the Module are organized in two groups of 8, each one with independent connection to one MBEE and one PSU. As shown in Figure 4, the MBEE is a large PCB located just on the back side of the relevant DAs, thus facilitating the interconnections to them. The main tasks of the MBEE are the following:

- time tagging
- trigger validation and filtering
- pedestal subtraction
- common noise subtraction
- energy reconstruction
- event threshold application
- housekeeping data collection.

The operating principle of the MBEE is the following: when the charge collected at one anode exceeds a programmable threshold in one of the ASIC channels in the FEE, a trigger signal is forwarded to the MBEE where a time tag (based on the 1 MHz clock count provided by the ICU) is instantaneously generated. The trigger is also propagated directly from one ASIC to all the ASICs on the respective detector half and they all freeze their current signal. The MBEE requests the

trigger map from all the ASICs on this detector half and validates if only one or two adjacent anodes triggered. If the event passes this selection criteria, the "A/D conversion" command is sent from the MBEE to the ASIC and the conversion is carried out (inside the OWB-1 ASIC), providing a 11-bit output per anode. Following the A/D conversion, the MBEE processing pipeline will be activated. The saved time tag will be added to the event package at the end of the processing pipeline. This pipeline is initiated 32 times within the MBEE FPGAs to allow processing of data from all 16 detectors simultaneously. The pipeline is designed such that the processing time within each step is the same and shorter than the A/D conversion time of a following event. In this way, the data processing in the MBEE does not inflict any additional dead-time and the pipeline is always ready for the next event.

A more extensive description of the MBEE and its development status is provided in Xiong et al.[15] and references therein. The MBEE is being prototyped at the University of Tuebingen. A photo of the board is shown in Figure 10.

The Power Supply Unit receives a low voltage input from the Power Distribution Unit hosted in the ICU and transforms it into the required power lines for the SDD, the FEE and the MBEE: 1.8 V, 3.3 V, 5V, 120 V and 1300 V. The PSU are hosted in a piggy-back configuration but in separate boxes with respect to the MBEE, to prevent EMC interference to the data processing in the FEE and MBEE. The total power dissipated in each Module (16x SDD, 16x FEE, 2x MBEE, 2x PSU) is 16.56 W, including the design maturity margin. To optimize the power dissipation towards the backside radiator of the Module, a thermal pad is inserted between the top of the PSU box and the backside cover of the Module frame. Both items (the PSU box and the thermal pad) are shown in Figure 4.

Detector and Collimator Frames

The Detector and Collimator Frames are key elements in the LAD Module design. Both of them are not just “bare mechanics”, but have functional tasks which are key to the fulfillment of the scientific requirements. The Detector Frame (DF) is in charge of supporting the DAs while efficiently transporting their produced heat to the backside radiator and not to the Collimator Tray, where it would cause thermoelastic distortions. Furthermore, the Detector Tray hosts the kinematic mechanical interface between the LAD Module and the support truss on the spacecraft, that should guarantee the inter-Module alignment and the alignment between the Modules and the satellite boresight.

The Collimator Frame (CF) has even more complex tasks, being a key element of the “optical system” of the LAD. In fact, the CF is designed in order to host and keep co-aligned the 16 capillary plate collimators, in all operational and thermal conditions. This is achieved through accurate machining, guaranteeing alignment using just the mechanical interface (“plug-and-play”), and through a clamping mechanism allowing for differential thermal expansion of the frame itself, the capillary plate and the optical filter, while maintaining the pore alignment. As an example, the capillary plate will have a degree of freedom, damped by a gasket, in the XY plane, to allow for expansion without causing bending or distortion.

An additional complexity of the design of both the Collimator and Detector Tray is the requirement of light tightness and vacuum venting, which is especially critical for the optical filter, as a differential pressure above a few mbar might cause its breaking, leading to the failure of the whole Module due to the resulting light contamination. Finally, all these requirements have to be accomplished by reducing the mass at its minimum. In fact, considering the large number of LAD Modules, any small increase in the mass of the Module will immediately multiply by 40 in the tight mass budget of the experiment.

As an example of the design activity being carried out by the LK Engineering and Frentech companies in Czech Republic (under a PRODEX contract managed by ESA), in Figure 6 we show the current design of LAD Detector Frame and the finite element analysis of a 2x2 cells prototype being developed to improve confidence in the design solutions.

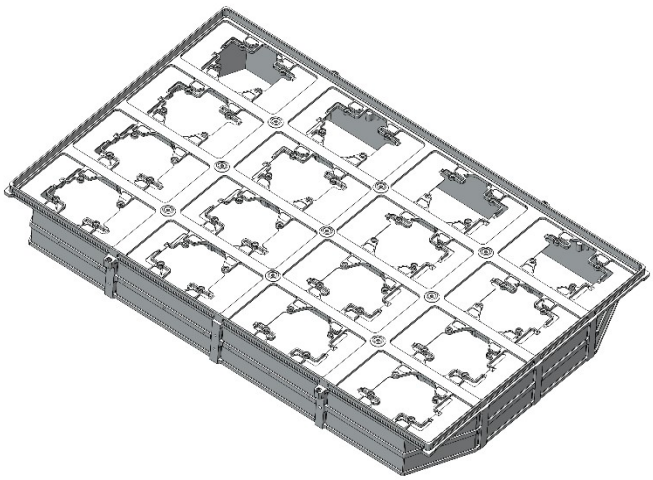

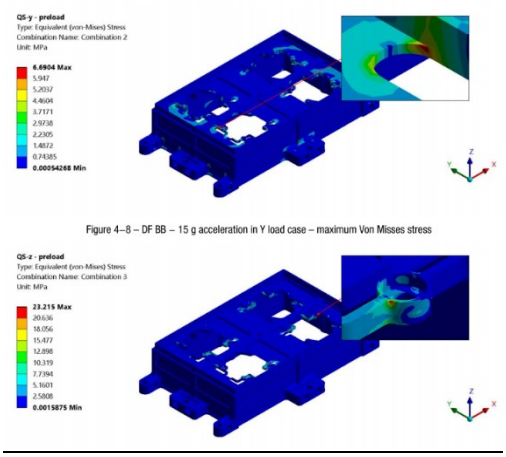

Figure 4–8 – DF BB – 15 g acceleration in Y load case – maximum Von Misses stress

Figure 6 Figures from the study of the Detector Frame. The left panel shows the current mechanical structure of the tray. The right panel shows finite element analysis of the 2x2 frame being prototyped.

Capillary collimators

The 1-degree (FWHM) field of view of the LAD is achieved through the collimation offered by the technology of the capillary plates. These are tiles of Lead-glass (with a required minimum Pb content of 37%) with thousands of coaligned micropores. This technology is derived by the manufacturing technology of the microchannel plates and, in the LAD design, they are monolithic 111 x 72.5 x 5 mm^3 tiles, with micropores of 83 µm diameter. The minimum required Open Area Ratio (OAR) is 70%, but the current technology has already demonstrated the capability to manufacture in-spec capillary plates with OAR in excess of 72% (it is worth noticing that this value has a direct impact on the effective area of the LAD).

The LAD is a collimated instrument. As such, the different Modules are required to be co-aligned. Any misalignment would effectively result in a smaller effective area and a larger field of view. The alignment requirement and strategy affect and drive several elements in the design. The field of view is limited by the individual pores of the capillary plates, which are then required to be co-aligned. The mounting of the 16 capillary plates within the Module collimator frame does not foresee individual fine-adjustments, it is achieved through a clamping mechanism, keeping the capillary pate and the optical filter in place in the recess of the frame designed to host them (Figure 7). This implies a requirement to the perpendicularity of the pore directions to the surface of the capillary plate, which is then mechanically interfaced ("plug-and play") to its hole in the collimator frame. The 16 capillary plates inside a Module are also required to be co-aligned one another, which imposes a stringent requirement on the accuracy of the machining of the collimator frame. Similarly, the 40 Modules on the LAD truss have to ensure a proper co-alignment, withstanding the launch loads and thermo-elastic distortions. As the interface between the LAD provision and the System is the Module (integration and alignment on the spacecraft truss is under the responsibility of the Prime Contractor of the spacecraft), the alignment budget is split between the Module and the Spacecraft. The overall alignment budget of the LAD is 2.1 arcminutes (99.7% confidence), which is then broken down and assigned to the individual components. The allocation to the module is described in Table 2.

Table 2 The alignment budget allocated to the LAD Module. The capillary plates collimators are briefly indicated as MPO (Micro-Pore Optics)

Item	Value [arcmin]	Condition
MPO INTERNAL TO MODULE	0.80	1σ
MPO mean pore axis to MCP surface	1.00	1σ
MPO pore axis distribution	1.00	1σ
Module thermoelastic deformations	0.17	1σ
TOTAL	**1.634**	**1σ**

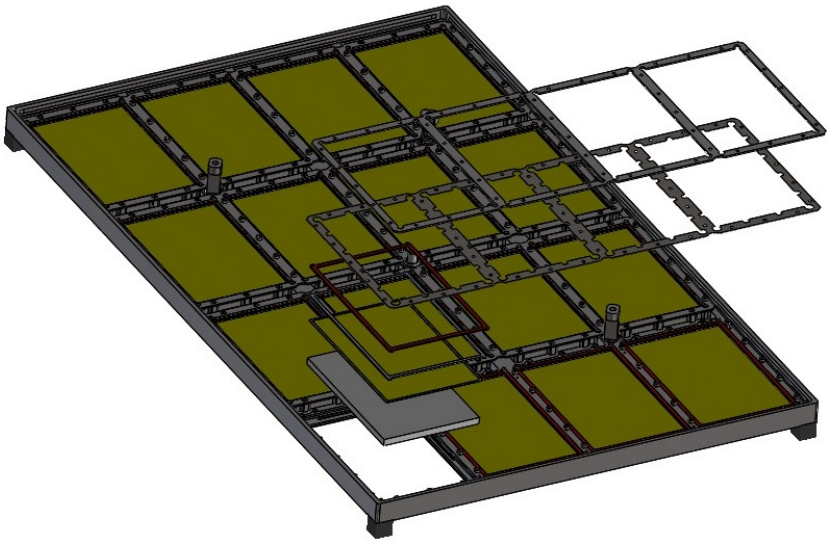

Figure 7 An exploded view of the Collimator Tray, showing the position of the capillary plate collimator (grey tile), the optical filter (green) and their clamping mechanism.

The alignment of the LAD elements is important to preserve the effective area within requirements. However, this element has to be traded-off against the response stability of the instrument. In fact, the response of a geometrically ideal collimator is a nearly triangular function. In this case, any instabilities of the attitude control system of the spacecraft will effectively result in a linear variation of the effective area of the instrument, as the instantaneous pointing will lay at different locations within the field of view (that is, at different position of the triangular response of the collimator). The resulting effect would be a spurious modulation in the source counting rate, due to a modulation of the instrument effective area rather than to the intrinsic source variability. Preventing this effect, by reducing it below the sensitivity limit of the instrument, is achieved by combining the alignment requirements of the instrument with a response stability requirement of the attitude and orbit control system of the satellite. In this respect, a non-perfect angular response of the capillary plates, as due to a limited misalignment of the pores, of the tiles within the Module and among Modules will actually help, offering a flat-top angular response of the instrument, at the price of some percent of total effective area.

In Figure 8 we show the photograph of a full-scale prototype of the capillary plate, produced by the North Night Vision Technology (NNVT) company in Nanjing (China), the industrial partner for this component of the LAD experiment. In the same figure a measurement of the angular response ("rocking curve") at 4.5 keV, as measured at the INAF-IAPS X-ray facility in Rome. The flat-top angular response is clearly visible.

It is worth noticing that the LAD instrument onboard eXTP has to operate simultaneously with the SFA and PFA instruments. As a consequence, the overall alignment of the LAD has to guarantee the pointing of its maximum effective area in a direction co-aligned with the boresight of these other two instruments. This imposes a further alignment requirement between the LAD and the nominal boresight of the spacecraft and will require a specific calibration on ground and in orbit.

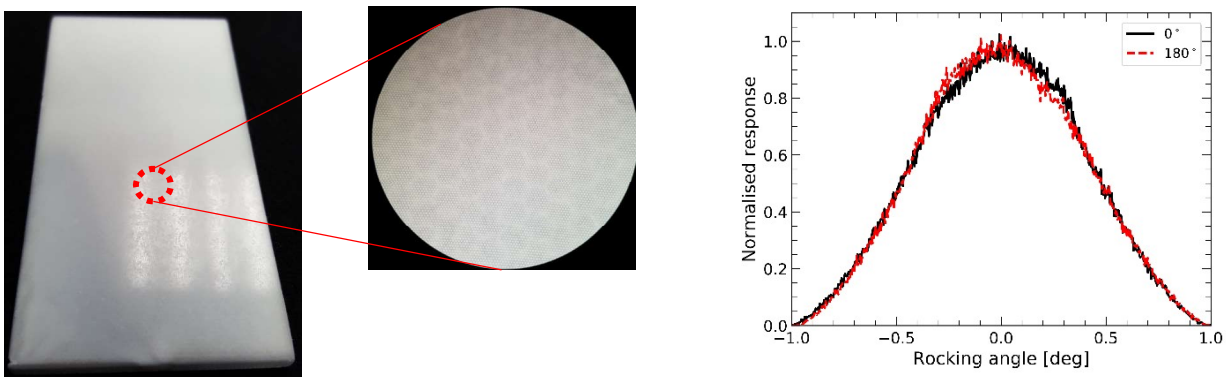

Figure 8 The capillary plate collimator of LAD. On the left: a photo of a prototype, with zoom-in showing the pores and the hexagonal domains structure. On the right: X-ray response at 4.5 keV as a function of the off-axis angle (rocking curve, the two data points correspond to the scanning in two directions to check for any biases in the measurement).

Optical filters

SDDs are excellent visible-light conversion devices, as such, in order to efficiently operate in low-noise conditions as X-ray detectors they have to operate in the dark. This requirement is achieved through design solutions when the mechanical structure of the Module is concerned. As an example, the coupling between the Detector Tray and the Collimator Tray is designed such as to have a light trap, yet allowing adequate venting holes. However, when the X-ray entrance window is concerned, the requirement of a >85% X-ray transparency can only be achieved through the use of a thin optical filter. The requirement on the optical transparency is driven by the scientific requirement of a negligible additional noise (due to the additional leakage current) with respect to the noise due to the intrinsic leakage current of the SDD. This translates into a requirement of a transparency $<10^{-8}$ in the IR/VIS/UV range. The filter is designed as a 112.4 x 73.9 mm^2 monolithic, 2 μm think polyimide foil, with a 150 nm Aluminum film on each side. To reduce the blocking factor to the detector entrance window, the filter is self-standing, with no mesh. A 100 μm Nickel or 400 μm Silicon frame (to be selected on the basis of tests) provides support and tensioning on the filter perimeter. The filter has been developed in house at the IHEP-CAS institute, based on the heritage of the HXMT filters[16]. A transfer to an external company implementing the same technology is ongoing, in view of the mass production needed for the LAD.

The LAD filters are being jointly developed by IHEP and INAF-OAPa[20]. Several full-scale prototypes have been developed and are undergoing functional, performance and qualification tests. These include: pinhole, X-ray transparency, infrared/optical/UV blocking (including a bright-Earth test), thermal-vacuum cycling, vibration, atomic oxygen tests (in cooperation with ESA), static differential pressure. In Figure 9 we show the filter prototype while running the differential pressure test. A more extensive discussion about the requirements, the design and the tests of the LAD optical filter may be found in Lo Cicero et al.[17].

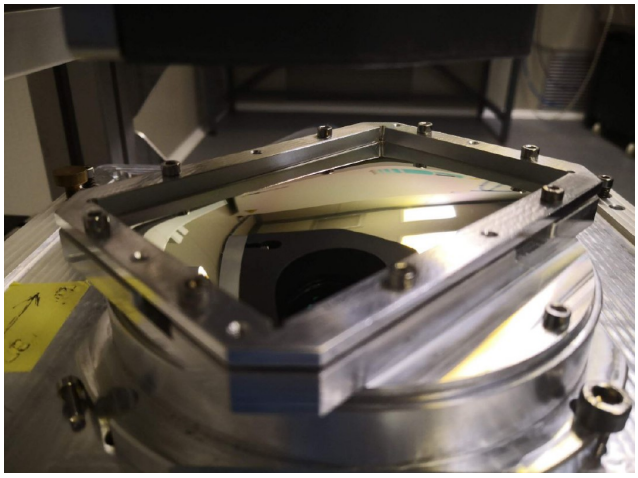

Figure 9 The prototype of the optical filter during the differential pressure test at the INAF laboratories.

3.2 The Panel Back End Electronics and Instrument Control Unit

PBEE – Panel Back End Electronics

The Panel Back-End Electronics (PBEE) handles all events from the individual modules of one of the two detector panels. It is the heart of the data acquisition and signal processing, located between the individual modules and the Data Handling Unit (DHU, part of the ICU) on the satellite bus. The main tasks of the PBEE are:

- Interfacing the MBEEs
- Collecting and buffering the event packets
- Differential time assignment
- Reformatting the data to binned data depending on the observation mode
- Transferring the data to the DHU
- Collection of housekeeping (HK) data and creation of HK packets.

The interface between PBEE and DHU is a fully compliant SpaceWire interface, runnnig at 100 MHz.

The four PBEE boxes will be accommodated in the spacecraft and each of them will interface 10 Modules, in a 4-quadrant configuration (see Figure 3).

ICU – Instrument Control Unit

The Instrument Control Unit is the main controlling element of the LAD instrument. It provides the interface to the spacecraft OBDH and it controls all LAD instrument sub-systems via SpaceWire. The ICU includes three components: the Data Handling Unit (DHU), the mass memory and the Power Distribution Unit (PDU). The tasks performed at the level of the ICU involve telecommand execution and distribution, access to mass memory, time distribution, data processing and compression, HK collection, instrument health monitoring and calibration tasks.

The ICU will manage the telemetry generated by the LAD instrument. The LAD event data will have a double structure: standard events (for sources dimmer than 0.6 Crab) will have a variable event packet from 58 to 80 bit/event; high rate events (for source intensity >0.6 Crab) will have 44 bit/event. Transmitting all events to ground, the instantaneous telemetry rate generated by the LAD will of course depend on the specific intensity of the target source. However, the average telemetry allocation for the LAD has been dimensioned by considering the minimum requirement of a sustained observation of 1 Crab sources. In this case, the average telemetry rate generated by the LAD is 3.1 Mbps, including event data, scientific ratemeters and housekeeping data.

As a single point of failure, the ICU is in cold redundancy. At its heart is the Data Handling Unit where the scientific data is compiled, processed and compressed. A quad-core GR-740 Leon-4 processor (not under ITAR restrictions) was chosen for the task to run the onboard software due to its additional flexibility when compared to a hardware only architecture, i.e. a state-machine. The DHU collects the data from the PBEEs via a SpaceWire interface PCB, performs the selection and formatting tasks depending on the selected observation mode and commits the data to the mass memory in a compressed format. Besides the routing and execution of telecommands, the ICU can run macro commands for several tasks, including on-board calibration and the individual sequenced switching of the MBEEs in the engineering modes.

The PBEE and the ICU boards are being prototyped in the framework of the development of a Demonstration Model of the LAD. The prototypes being developed at University of Tuebingen are shown in Figure 10.

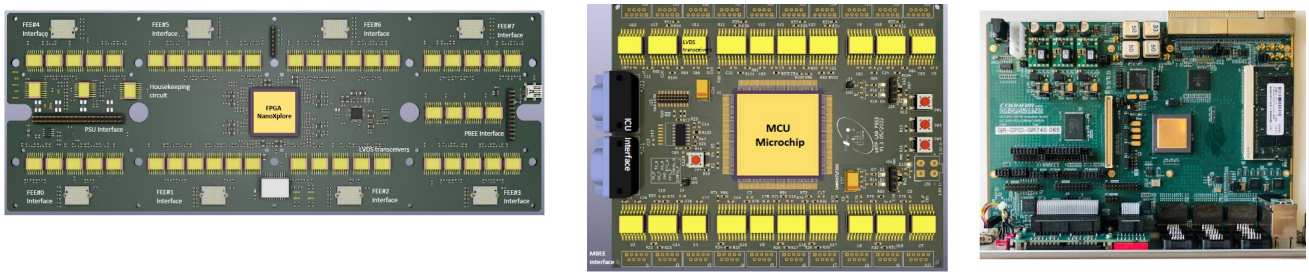

Figure 10 Prototypes of the digital electronics of the LAD, in preparation at the University of Tuebingen. Left: Module Back End Electronics. Center: Panel Back End Electronics. Right: Instrument Control Unit. See Xiong et al.[15] for further details.

4. EXTP RADIATION ENVIRONMENT AND LAD OPERATING TEMPERATURE REQUIREMENT

Due to the sensitivity of the SDDs to radiation damage in orbit, which causes increase of the detector leakage current and a consequent worsening of the spectral resolution, the assessment of the eXTP radiation environment is a primary task for the LAD development study. During the initial study of the LOFT mission, as well as during the eXTP phase A, the most reliable model for an equatorial low-Earth orbit (LEO) was the AP8 model, being the newer AP9 model largely overestimating the environment at equatorial LEO. This model was indeed adopted, with large margins, to perform the analysis of the expected LAD radiation damage in its 5 years operation in orbit, resulting in an end-of-life (EOL) requirement on the detectors operating temperature of <-11°C, enabling to compensate for the increased leakage current at EOL and meet the requirement on the spectral resolution.

Recently, new data have become available in this field: (a) the data of the particle monitor onboard the Chinese HXTM mission provided an accurate map of the South Atlantic Anomaly at low altitudes and (b) a study commissioned by ESA (RENELLA – Radiation ENvironment at Extremely Low Latitude and Altitude) led to a uniform and complete analysis of all available data from past spacecrafts and produced an updated model, the LARB model[18] (Low Altitude Radiation Belt model). The LAD team made a thorough analysis of the new data and LARB model, together with a reanalysis of the BeppoSAX data, already used in the previous assessment. It turned out that the LARB model offers indeed a suitable description of the radiation environment at the eXTP orbital parameters.

Using the LARB model, a reassessment of the operating temperature requirement (flow-down from the spectral resolution requirement of 260 eV FWHM at 6 keV) was carried out. The result is synthetically shown in Figure 11. This plot shows the LAD SDD operating temperature requirement as a function of the mission lifetime for different conditions of intrinsic leakage current (i.e., the Beginning of Life value). As expected, with the harsher radiation environment determined in the new analysis, the impact of the BoL leakage current becomes uncritical as the mission lifetime increases. At the time of the nominal mission EoL (5 years), the curves related to the different starting leakage current levels differ by just a few degrees, well within the margins applied to the operating temperature at this stage of the study (typically, 5°C on the radiation model plus 5°C on the thermal analysis). For the current value of the BoL

leakage current requirement (150 pA/cm^2), the SDD operating temperature requirement was assessed as <-30°C, including margin. It is worth noticing that this value aims at meeting the spectral resolution requirement at EoL, the plot shows that in the first 2-3 years of the mission the <-30°C operating conditions will lead to a performance significantly better than the requirement.

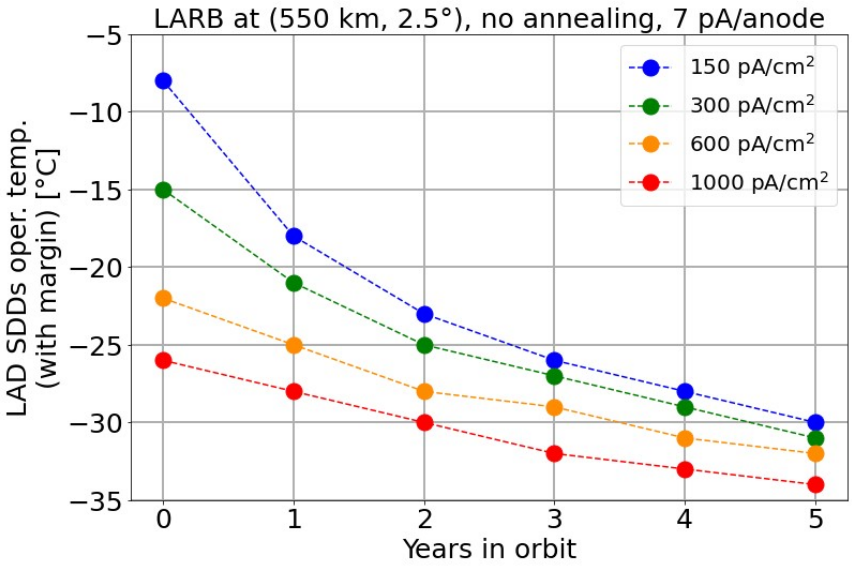

Figure 11 Analysis of the sensitivity of the LAD operative temperature requirement, as a function of the lifetime in orbit and the detector leakage current at the beginning of life.

5. UPDATED THERMAL DESIGN

The major update of the SDD operating temperature requirement, from the earlier <-11°C to the current <-30°C, imposed by the revised radiation environment modelling had a major impact on the thermo-mechanical model of both the LAD and the spacecraft. Considering that the LAD Module is passively cooled and it has to operate in largely different conditions of Sun Aspect Angle and attitude, both the Module design and the spacecraft accommodation and thermal interfaces had to be revised. The thermal simulations were carried out using a complete model of the spacecraft and both detailed and simplified models of the Module. In fact, given the large number of Modules in the LAD, a thermal model of the spacecraft including a detailed model of the Module would be computationally unmanageable. The analysis was thus carried out using a 3-step approach. First, a thermal model of a "stand-alone" Module was used with just a Sun-shield, to identify the main thermal boundary conditions for the Module and use them to optimize the detailed Module design. Second, a complete model of the satellite was adopted, with a simplified thermal model of the Module, to assess the main thermal conditions of the Modules at different locations. Finally, the detailed model of the Module was placed in different specific positions in the LAD layout, identified as representative of "thermal families" of LAD Modules. These steps are illustrated in Figure 12.

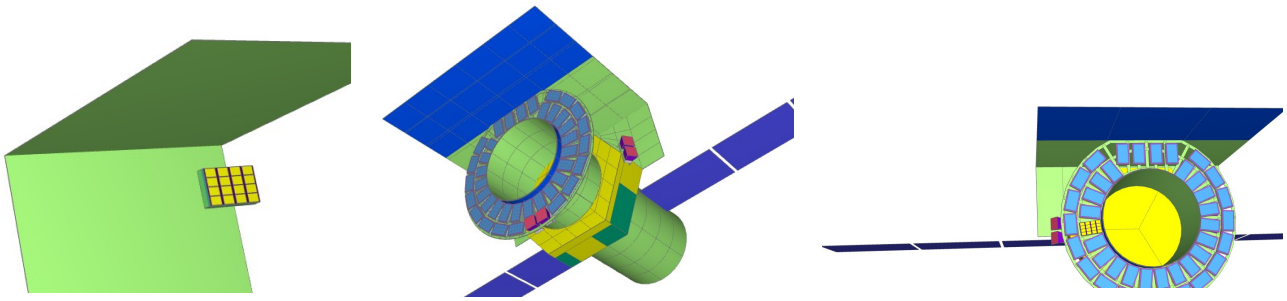

Figure 12 The thermal models of the LAD and the eXTP satellite. Left panel: the simplified model including one LAD Module and the Sun shield only. Center: the complete satellite model, including simplified thermal models of the Module. Right: the complete satellite model, including one detailed LAD Module and 39 simplified LAD Modules The detailed Module was iteratively placed at different representative locations in order to achieve more accurate thermal analysis at all LAD locations.

The result of this first analysis allowed indeed to identify groups of Modules with similar thermal behavior. The boundary conditions primarily affecting the thermal behavior of the different Modules are the presence of the Sun shield, that irradiates part of the Sun heat from its back side and the different viewing angle of the backside thermal radiator of each LAD Module, depending on their positions on the spacecraft. In fact, some of them always see the open sky, some of them are partially blocked by the central cylinder and some of them are blocked by both the cylinder and the Sun shield. In Figure 13 we show the relative thermal behavior of the LAD Modules in a specific condition (here the Hot Case). The labels A through F identify the different thermal groups.

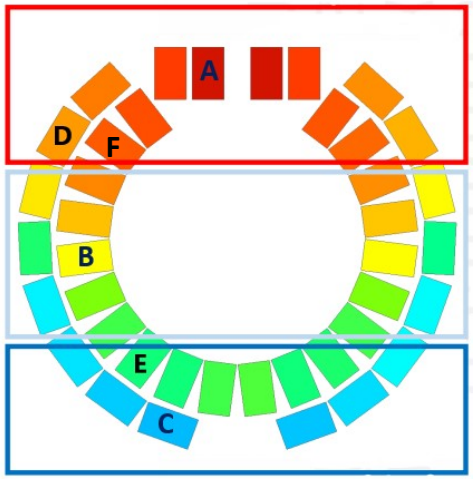

Figure 13 The relative temperature distribution of the LAD Modules in the configuration shown in Figure 12. Red is hottest, green is coldest. Boxes identify the main thermal groups.

The thermal conditions illustrated above proved to be out-of-spec of the LAD, thus requiring an update in the thermal design of the spacecraft. This was indeed implemented by adopting 2 external radiators, in charge of providing a supplementary thermal path for the dissipation of the 12 Modules closer to the Sun shield. This solution proved indeed to be effective, leading to an in-spec configuration. In Figure 14 we show the updated spacecraft model, with the resulting thermal distribution of the Module relative temperatures. As expected, in this configuration the hottest Modules become those at the boundary of the two sets of Modules connected to the two external radiators (6 on each side).

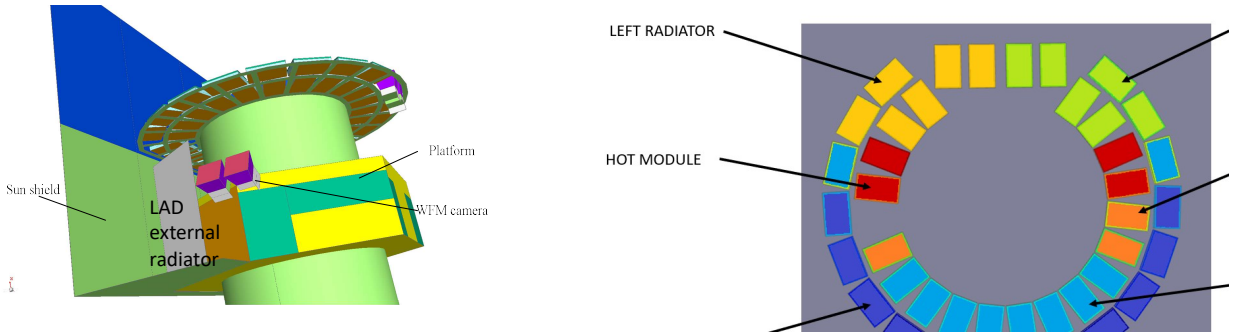

Figure 14 Left: the satellite design including the LAD external radiators (one of the two is visible in gray). Right: the relative temperature distribution in the configuration shown on the left.

In this configuration the thermal simulations were run in all representative thermal conditions and the operative temperature requirement of the LAD was met. In Figure 15 we show the results in one representative case, the Hot Case. The box-plot on the left reports the temperature ranges of different components of the Module over one orbit, showing the detectors (first boxplot from the left) to be in-spec. The plot on the right shows the orbital variability of the 16 detectors in a Module. While the temperature stays always below the requirement, the orbital variability is in a ±7°C range, requiring an equalization of the response of the different detectors before combining them in scientifically meaningful data.

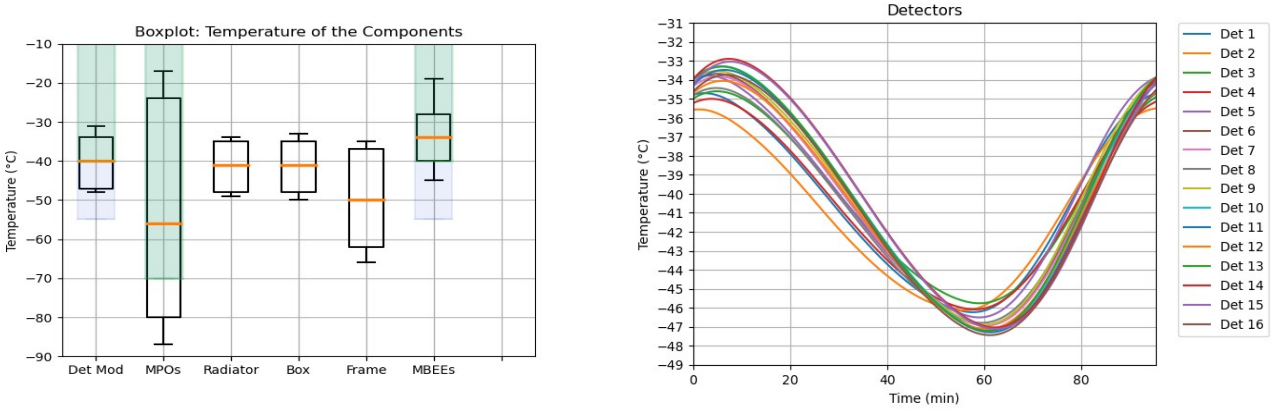

Figure 15 Temperature variations on the orbital timescale in the Hot Case. Left: box-plot showing the maximum (box) and average (orange line) temperature of different Module components. Right: orbital variation of the 16 detectors in a Module.

The analysis shown in Figure 15 predicts a wild temperature orbital variation of the outermost component of the LAD Module, the capillary plate collimator. These are certainly challenging operating conditions, yet compliant with the thermal requirements of this component. It remains to be verified the compliance with the alignment requirements, also including the Module frames and the clamping mechanism.
A more extensive discussion of the LAD thermal analysis may be found in Lombardi et al.[19].

6. CONCLUSIONS AND OUTLOOK

The Large Area Detector will be one of the European contributions to the eXTP mission, under the responsibility of the European eXTP Consortium. In particular, the LAD design and development is currently coordinated by the Italian Space Agency (ASI), with important contributions from Germany, France, Switzerland, Poland, Czech Republic and Austria in Europe and from China.

The LAD experiment is currently at the end of its Phase B1 study, with the Instrument System Requirements Review planned before the end of 2022. The Phase B2 is instead expected to be completed by the end of 2023 with the Instrument Preliminary Design Review (I-PDR).

Among the key tasks of Phase B is the demonstration of the maturity of the technology and of the design. To this purpose, all critical components and subsystem of the LAD are being prototyped and demonstrated. Before the end of Phase B, a Demonstration Model of the Module (full scale), the PBEE and the ICU is foreseen, with an end-to-end bench integration of all subsystem, to demonstrate their interfaces and compatibility. We therefore expect to reach a Technology Readiness Level 5-6 by I-PDR. A crucial aspect of this development is taking care of the export limitations to China. In this respect, the LAD design is being developed by adopting only components, materials and processes which are not produced in the US and for which no export restrictions are known also at European level. This cautionary approach should be able to prevent any export-related delivery issues at the later phases in the program.

The current status of the development is in line with the above planning and the Phase B is expected to be successfully completed in compliance with the current schedule of the project.

ACKNOWLEDGEMENTS

The Italian authors acknowledge funding support by the Italian Space Agency (under agreement n. 2020-3-HH.0 and ASI-INAF n.2017-14-H.O) and INFN (project XRO - X-ray Observatories). The Chinese team acknowledges support by the Chinese Academy of Sciences through the Strategic Priority Research Program, Grant No. XDA15020100. The German team acknowledges support from the Bundesministerium für Wirtschaft und Technologie through the Deutsches Zentrum f˙ur Luft- und Raumfahrt e.V. (DLR) under the grant number FKZ 50 OO 1902. The Polish team acknowledges FNP grant POIR.04.04.00-00-5C65/17.
The LAD team is grateful to the ESA Radiation Department and to the RENELLA project, in particular Alex Stefanescu and Hugh Evans at ESA, Fan Lei at RadMod Research, Pete Trescott at Kallisto Consultancy and Daniel Heynderickx at DH Consultancy, for making the LARB model available ahead of its official release and providing key support to enable the LAD radiation environment analysis.

REFERENCES

[1] A. Di Marco et al. 2022, these proceedings and references therein.
[2] A. Watts et al. 2019, Science China – Physics, Mechanics and Astronomy, Vol. 62 No. 2: 029503
[3] A. De Rosa et al. 2019, Science China – Physics, Mechanics and Astronomy, Vol. 62, No. 2: 029504
[4] A. Santangelo et al. 2019, Science China – Physics, Mechanics and Astronomy, Vol. 62 No. 2: 029505
[5] J.J.M. in ‘t Zand et al. 2019, Science China – Physics, Mechanics and Astronomy, Vol. 62 No. 2: 029506
[6] M. Weisskopf et al. 2016, Proc. SPIE 9905, 990517
[7] M. Hernanz et al. 2022, these proceedings.
[8] S.N. Zhang et al. 2022, Handbook of X-ray and Gamma-ray Astrophysics, to be submitted
[9] S.N. Zhang et al. 2019, Science China – Physics, Mechanics and Astronomy, 62, 029502
[10] A. Vacchi et al. 1991, NIM A 306, 187
[11] A. Rachevski et al. 2014, JINST 9, P07014
[12] A. Di Marco et al. 2022, these proceedings and references therein.
[13] D. Baudin et al. 2022, IEEE Trans. on Nuclear Science, Vol. 69, No. 3, p. 620
[14] F. Bouyjou, O. Gevin, O. Limousin, and E. Delagnes, 2017, IEEE Trans. on Nuclear Science, Vol. 64, No. 4, p. 1071
[15] H. Xiong et al. 2022, these proceedings.
[16] Y. Chen et al. 2020, Science China – Physics, Mechanics and Astronomy, 63, 249505-2
[17] U. Lo Cicero et al. 2022, these proceedings.
[18] https://nom.esa.int/models/trep_larb
[19] G. Lombardi et al. 2022, these proceedings.
[20] T. Chen et al. 2020, "Optical thermal filters for eXTP: manufacturing and characterization." SPIE 11444
[21] W. Chen et al. 2020, Proc. SPIE 11444, 114442E-1